Non-Line-of-Sight Three-Dimensional Imaging with a Single-Pixel Camera

G. Musarra, A. Lyons, E. Conca, Y. Altmann, F. Villa, F. Zappa, M.J. Padgett, and D. Faccio
Phys. Rev. Applied 12, 011002 – Published 18 July 2019

Letter | Editors' Suggestion | Featured in Physics

Non-Line-of-Sight Three-Dimensional Imaging with a Single-Pixel Camera

G. Musarra,[1,*] A. Lyons,[1] E. Conca,[2] Y. Altmann,[3] F. Villa,[2] F. Zappa,[2] M.J. Padgett,[1] and D. Faccio[1,†]

[1] *School of Physics & Astronomy, University of Glasgow, Glasgow G12 8QQ, United Kingdom*

[2] *Dipartimento di Elettronica, Informazione e Bioingegneria, Politecnico di Milano, 20133 Milano, Italy*

[3] *School of Engineering and Physical Sciences, Heriot-Watt University, Edinburgh EH144AS, United Kingdom*

(Received 6 March 2019; published 18 July 2019)

Real-time high-resolution three-dimensional (3D) reconstruction of scenes hidden from the direct field of view is a challenging field of research, with applications in real-life situations related, e.g., to surveillance, self-driving cars, and rescue missions. Most current techniques recover the 3D structure of a non-line-of-sight (NLOS) static scene by detecting the return signal from the hidden object on a scattering observation area. Here, we demonstrate the full color retrieval of the 3D shape of a hidden scene by coupling back-projection imaging algorithms with the high-resolution time-of-flight information provided by a single-pixel camera. By using a high-efficiency single-photon avalanche-diode (SPAD) detector, this technique provides the advantage of imaging with no mechanical scanning parts, with acquisition times down to the subsecond range.

DOI: 10.1103/PhysRevApplied.12.011002

The identification of scenes hidden from the direct line of sight, as happens for objects hidden behind an occluder or wall, is a challenging imaging task, with applications in defence, surveillance, and self-driving vehicles [1]. Non-line-of-sight (NLOS) imaging has been demonstrated by using radar systems [2], wave-front shaping [3], and speckle correlation [1,4,5] and recently even with passive cameras capturing light originating from behind a wall, using an ordinary digital camera [6]. Most approaches in this field have demonstrated how to identify the hidden scene by collecting the light scattered back by hidden objects with a system similar to light detection and ranging (LIDAR) by using the time-of-flight information of the back-scattered signal [7–11]. This technique typically involves a pulsed laser beam pointed on a scattering surface, producing a spherical wave propagating into the hidden scene. When the spherical wave hits the hidden object, the light is then scattered back toward the scattering surface. Collection of the third-bounce echo scattered from the hidden object allows the detection and identification of the hidden scene by advanced three-dimensional (3D) reconstruction algorithms [12]. Past results have demonstrated how this technique can be used for tracking a moving hidden object even over large distances [13,14] and for the retrieval of the 3D shape of a static hidden object by using back-projection imaging algorithms [12,15] or ellipsoid-mode decomposition for multiple hidden objects [16]. Alternative methods aimed at simplifying or increasing the speed of LIDAR-like NLOS imaging rely on two-dimensional (2D) continuous illumination [17], deep learning [18], and confocal illumination and/or collection [19]. The multiple-bounce back-scattered signal is typically very weak, so these techniques require high temporal resolution and high-speed single-photon cameras with a high detection efficiency.

However, one of the main limitations of current NLOS imaging systems is the finite temporal resolution of the detectors, which in turn determines the spatial resolution of the retrieval and thus the ability to reconstruct satisfactorily the 3D structure of the hidden scene. Furthermore, the complete 3D retrieval of the hidden scene often requires prohibitive time resources with the 3D imaging of a moving object, although progress is being made to reduce the acquisition and reconstruction times [6,19], with the goal of reaching times in the second or even subsecond range. Additionally, the spatial resolution of the retrieval can be improved by using iterative back-projection algorithms that, however, typically require longer computational times [20,21].

Another rapidly evolving imaging technique is based on so-called single-pixel cameras [22]. Standard 2D single-pixel imaging systems recover images by projecting an array of patterns onto the scene and detecting only the total reflected- or transmitted-light intensity, for which a single pixel is sufficient. The computational image reconstruction can then be achieved by computing a weighted

*2376730m@student.gla.ac.uk
†daniele.faccio@glasgow.ac.uk

sum of all the illumination patterns, where the weight of each pattern is given by the corresponding measured intensity level. This technique can also be extended for use in, e.g., microscopy [23], imaging through scattering media [24], and terahertz imaging [25] or full 3D LIDAR [26–28].

Although this technique requires many consecutive measurements, the consequent long acquisition time required for high-spatial-resolution images can be significantly reduced by applying compressive sensing [25,29,30]. More importantly, the technique provides more flexibility in choosing the optimal (single-pixel) detector for the imaging challenge being addressed. Of relevance to this work, this implies that we can choose a single-pixel detector with an enhanced temporal response and build upon the typically better temporal resolutions that are available in single-pixel format (timing resolutions down to picoseconds), when compared to technologies involving camera and/or single-photon avalanche-diode (SPAD) arrays.

In this work, we demonstrate full 3D retrieval of hidden scenes by using a time-resolved single-pixel camera. The choice of a single-pixel-camera approach allows us to use optimized (sub-30-ps impulse-response function) single-photon detectors in combination with a digital-mirror device (DMD) so as to remove the need for any scanning components while building upon the 20-kHz refresh rate of the DMD and the high single-photon sensitivity to reduce acquisition times with good reconstruction fidelity. By employing a white-light laser, we extend the technique to achieve the full red-green-blue (RGB) color retrieval of noncooperative hidden objects and by choosing high-efficiency SPADs we also achieve subsecond acquisition times.

Figure 1(a) shows the experimental setup: the single-pixel camera is composed of a camera-lens objective (8 mm focal length, $f/3.5$) that images a 50×50 cm^2 portion of a scattering wall onto a DMD (placed 1.16 m from the wall). The DMD then projects only selected portions (masks) of the image onto a single-pixel single-photon detector through a microscope objective. The single-photon detector therefore acts as a bucket detector and has a 30-ps impulse-response time and an area of 57×57 μm^2. The DMD masks have 20×20 pixels, corresponding to 2.6×2.6 cm^2 pixel areas on the scattering wall. The single-photon data are recorded in time-correlated-single-photon-counting (TCSPC) mode triggered by the illumination laser, as a histogram of photon arrival times, with 4096 time bins of 6.1-ps duration each. The laser is directed on the scattering wall 10 cm to the right of the field of view of the single-pixel camera, producing a first scattered spherical wave. Part of the spherical wave hits the hidden object, which in turn scatters back into the field of view, where it is captured by the time-resolved single-pixel camera. The intensity at a

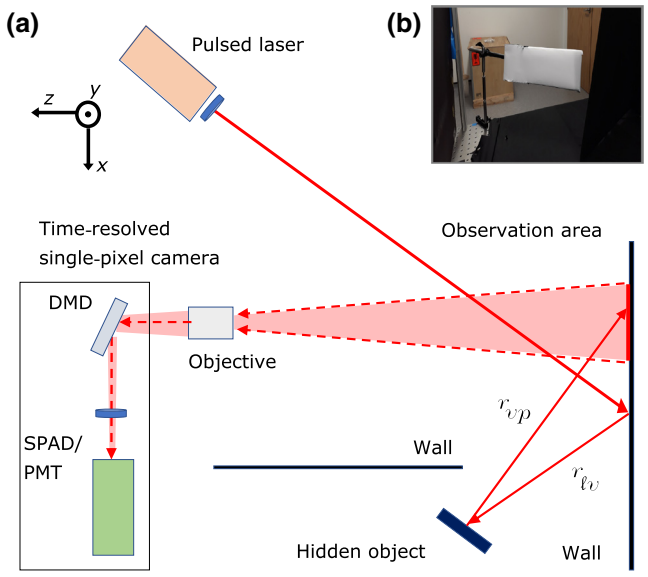

FIG. 1. The schematics of the experimental setup for NLOS imaging. (a) A pulsed laser scatters on a scattering surface, producing a spherical wave in all the surrounding area. The DMD is imaging a 50×50 cm^2 area of the scattering surface and the time-resolved single-pixel camera collects the signal back-scattered from the target in the hidden scene by temporal histograms. We collect the signal scattered back by the hidden target by sequentially collecting light from each of the 20×20 pixels either by raster-scan masks or by Hadamard masks. (b) The noncooperative single-object scene used for ultrafast NLOS imaging.

given pixel $(x', y', z' = 0)$ on the observation area at an arrival time t is given by the voxels of the object that could contribute to the signal, described as follows:

$$I(x', y' z' = 0, t) = \int_{x,y,z} \frac{I_0 \delta(tc - r_{\ell v} - r_{vp})}{r_{\ell v}^2 r_{vp}^2} dx dy dz, \quad (1)$$

where I_0 is the initial intensity of the spot on the wall and the delta function describes the propagation of the light from the laser spot to the target and back to the observed pixel. Here, tc is the distance covered by light traveling at speed c in time t, $r_{\ell v}(x, y, z) = \sqrt{x^2 + y^2 + z^2}$ is the distance between the object voxels and the laser spot, and $r_{vp}(x, y, z, x', y', z' = 0) = \sqrt{(x - x')^2 + (y - y')^2 + z^2}$ is the distance between the portion of the object and the observed pixel. The δ term encodes the object shape through the time-of-flight signal created in reflection from each coordinate point of the object and the $1/r^2$ terms encode the intensity decay with distance due to diffusive reflection from the wall and object.

We then explore various imaging scenarios, testing different objects and DMD mask choices. For the first scenario, we investigate a hidden scene of two cooperative objects, i.e., a highly reflective tin-foil 7.62-cm-diameter cylinder and a 2.54-cm-diameter mirror, placed at different

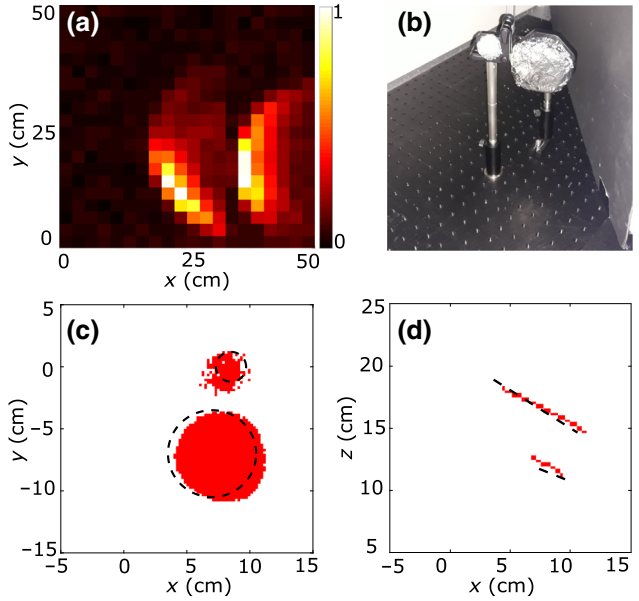

FIG. 2. A cooperative two-object scenario for a NLOS single-pixel camera based on a PMT detector. (a) The return signal produced by the two hidden objects and retrieved by raster-scan imaging onto the DMD and collection of the signal on the single-pixel detector in the time frame $t = 7.1$ ns. (c),(d) 3D shape retrieval of the hidden scene in (c) the x-y plane and (d) the x-z plane after applying a back-projection imaging algorithm. The dotted line represents the actual position of the targets. To facilitate the visualization, the reflectivity is normalized to the local maxima value. The objects to be recovered are two round targets of 2.54 cm and 7.62 cm diameter at a varying depth and tilted. The voxel dimension is $0.2 \times 0.2 \times 1$ cm^3 for an area to investigate of $20 \times 20 \times 100$ cm^3. The threshold used for the retrieval is 0.89.

positions and distances from the wall [see Fig. 2(b)]. We use a 120-fs pulsed laser at 808 nm wavelength with a repetition rate of 80 MHz and an average power of 800 mW. We collect the third-bounce echo with a simple raster-scan acquisition on the DMD, one 2.6×2.6 cm^2 imaging pixel at a time, and collect the reflected light onto a photomultiplier tube (PMT, hybrid photodetector HPM-100-07, Becker & Hickl, 4% efficiency at 808 nm) with optimized temporal response (the measured total impulse-response time is 27 ps FWHM). The acquisition time is set by the amount of the back-scattered signal detected by the sensor. In this case, the acquisition time is 10 s per mask (i.e., pixel) for a total acquisition time of 66 min. Figure 2(a) shows one time frame of the collected third-bounce echoes of the two hidden objects.

We proceed with the retrieval of the 3D shape of the hidden objects by applying the back-projection imaging algorithm first introduced by Velten *et al.* [12,20]. Although faster retrieval methods are available (see, e.g., Ref. [15]), our primary focus here is on the hardware rather than on the retrieval software. Regarding the time-of-flight evaluation, we consider the moment when the laser hits the wall as the zero time reference. We therefore divide the 3D space into 10^6 voxels and we calculate the likelihood of the target being localized on each voxel by using the time of flight t_p that the light takes to cover the distance $r_{\ell v} + r_{vp}$. The relation $ct_p = r_{\ell v} + r_{vp}$ indicates that all the possible contributions to a given pixel lie on the surface of an ellipsoid the foci of which are the laser spot and the pixel position. The ensemble of the 400 temporal histograms overlaps at the scattering object position and thus encodes the 3D geometry of the hidden objects. We assign the likelihood of a voxel by summing the intensity of the pixels that could have received any contribution from the voxel. Following Ref. [12], the final 3D shape of the object is improved by applying a Laplacian filter followed by a threshold selection on the data along the $\hat{z}$ direction of the voxel grid. This thresholding is applied to remove artifacts, e.g., blurring of the reconstructed object due to the limited projection angles of the imaging system and that make a relatively small contribution to the voxel probability distribution [16,31]. It is important to mention that artifacts can appear in the 3D reconstructed scene, mostly due to the ill-posedness of the inverse problem induced by the geometry of the sensing strategy (the limited field of view). Such artifacts can include blurred 3D structured and spurious objects not actually present in the scene. A high timing resolution (as used in this work) definitively improves the reconstruction performance and the proposed thresholding approach also seems robust to artifacts. However, more complex and robust computational methods might be needed for more challenging NLOS imaging scenarios, e.g., more complex objects, further away from the wall.

Figures 2(c) and 2(d) show the results on the x-y plane and on the x-z plane, respectively. The dotted line in each figure indicates the actual positions of the targets. Our results show that this technique provides an accurate 3D shape recovery of the hidden (cooperative) targets, although with relatively long acquisition times.

We then investigate a hidden scene of noncooperative objects with the same setup (Fig. 3). In this case, the scene to be recovered is a RGB-colored object, placed outside the direct line of sight [Fig. 3(b)], where each colored region has a rectangular shape of 20×9 cm^2. In order to retrieve the color information, we use a supercontinuum laser (SuperK EXTREME/FIANIUM, NKT Photonics, repetition rate 67 MHz, pulse duration approximately 10 ps, average power 100 mW in the 450–700 nm spectral range). For the RGB retrieval, we run a separate measurement for each of the three RGB colors, using corresponding bandpass spectral filters centred at of 490, 550, and 610 nm (40-nm bandwidth) after the laser source, with roughly 20 mW average power for each color. As above, due to the relatively low laser power, the optimal acquisition time is found to be 10 s per mask for an overall acquisition time of 66 min. Figure 3(a) shows the three return signals scattered

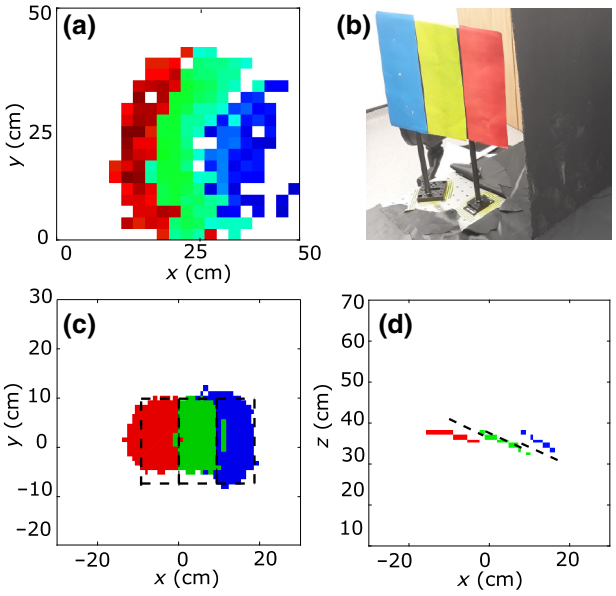

FIG. 3. A noncooperative objects RGB-colored scenario for a NLOS single-pixel camera based on a PMT detector. The red color corresponds to the recovered target by using the red spectral filter and so on. (a) The return signal produced by the hidden object by raster-scan acquisition. (b) The RGB-colored target. (c),(d) RGB retrieval of the 3D shape of the hidden objects in (c) the x-y plane and (d) the x-z plane after applying a back-projection imaging algorithm. The red color corresponds to the recovered target by using the red spectral filter and so on. The dotted black line represents the actual position of the target. We discretize the space in voxels of $1.4 \times 1.4 \times 1$ cm^3 for an overall area of $140 \times 140 \times 100$ cm^3.

back by the three RGB-colored targets at a time frame of 8 ns. Figures 3(c) and 3(d) show the reflectivity on the x-y plane and on the x-z plane, respectively: as can be seen, the retrieved 3D scene corresponds very closely to the ground truth (dashed lines).

The last scenario that we investigate is a noncooperative hidden object [a white paper rectangle of 24×10 cm^2; see Fig. 1(b)] aimed at the optimizing acquisition time. We achieve high-speed acquisition by using a high-efficiency (70% peak efficiency at 550 nm) SPAD detector [32] with a measured impulse-response function of 30 ps FWHM. The SPAD has a square active area of 57×57 μm^2 and we use a 75-mm-focal-length lens and a long-working-distance objective (magnification factor 50) to focus the light after the DMD onto the sensor. The high sensitivity of the detector allows a shorter acquisition time of 1 ms per mask, which in this case where chosen as the first 400 Hadamard patterns, with the goal of increasing the amount of collected light for each mask (50% of the pixels are always projected onto the detector for each mask). For each Hadamard pattern, one binary mask and its negative are used and combined, leading to a total of 800 patterns. This allows the total acquisition time to be reduced to only 0.8 s.

In this case, we use the same supercontinuum laser as in the previous scenario, with a power of 550 mW at 550 nm. As shown in Fig. 4(a), the collected third-bounce echo of the signal is affected by a low signal-to-noise ratio due to the short acquisition time. We therefore first apply a denoising algorithm similar to that used in Ref. [33], thus returning the signal shown in Fig. 4(b). To be precise, a cost function is defined, accounting for the forward model (including observation noise that is assumed to be Poisson distributed) relating the image sequence (or video) reaching the DMD and the set of temporal sequences recorded for each Hadamard pattern. The cost function also includes two penalty terms to promote temporal and spatial smoothness after denoising. This is enforced by using a spatial total-variation (TV) regularization, as well as a low-pass constraint on the Fourier transform of the temporal intensity profile of each pixel. This cost function is convex and the denoising step, i.e., the cost-function minimization, is performed using an alternating direction method of multipliers (ADMM) algorithm [34], as in Refs. [35] and [36]. Figures 4(c) and 4(d) show the retrieved reflectivity of the hidden objects on the x-y plane and on the x-z plane, respectively. Our results therefore show that this technique provides an accurate 3D shape of a hidden target even with

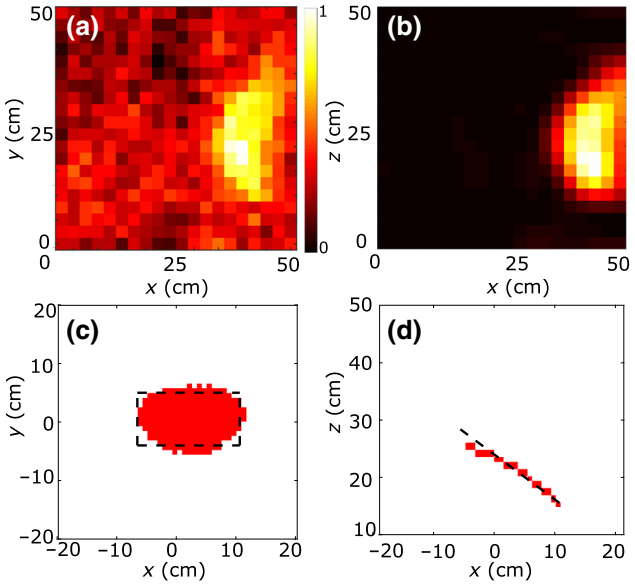

FIG. 4. The ultrafast NLOS single-pixel camera results. (a) The return signal produced by the hidden object by Hadamard acquisition at a time frame of 5.3 ns. (b) The return signal obtained by the preprocessing filter. (c),(d) Retrieval of the 3D shape of the hidden target in (c) the x-y plane and (d) the x-z plane after applying a back-projection imaging algorithm. The dotted black line represents the actual position of the target. The object to be recovered is a rectangular target of 24×10 cm^2. The voxel dimension is $1.4 \times 1.4 \times 1$ cm^3 for an overall of $140 \times 140 \times 100$ cm^3. The threshold used for the retrieval is 0.80.

subsecond acquisition times, with an average number of only 1.2 photons per pixel in each time frame (with a maximum peak photon number of approximately 10 photons per pixel).

In conclusion, the high efficiency and the high temporal resolution of single-pixel single-photon detectors allow us to accurately recover the 3D shape of hidden objects even with low-resolution masks of 20×20 pixels and no mechanical scanning parts.

The main limitation on the spatial resolution of the retrieval is due to the pixel size on the scattering wall. In our case, a pixel size of 2.6×2.6 cm^2 limits the temporal resolution to 60 ps due to the blurring of the pulse wave front as it crosses the 3.6-cm pixel collection area (taking the diagonal of the square pixel). This effectively corresponds to an uncertainty in the arrival time of the return pulse and, in analogy with standard LIDAR, will translate into an uncertainty of the object depth location that is half this value, i.e., 1.8 cm. This can be overcome by decreasing the pixel size; however, this is achieved at the cost of longer acquisition times due to the larger number of Hadamard patterns (or pixels to scan).

Overall, the ability to identify a hidden scene by the proposed approach is mainly determined by the time resolution of the detector and by the time required to acquire a significant back-scattered signal. The retrieval of hidden scenes still remains a challenging task, due to long acquisition times and low spatial resolution of the retrieval and computational sources, although significant steps have been made recently (see, e.g., Refs. [6] and [19]). We show a NLOS ultrafast imaging technology that can reliably recover the 3D shape in color of a scene with high spatial resolution by using single-pixel single-photon detectors with high temporal resolution. By using a high-sensitivity detector, this system is able to retrieve the shape of the hidden target with an acquisition time of 0.8 s, paving the way for real-time 3D shape recovery of hidden objects. The accurate 3D shape recovery of this system could be further improved by fully exploiting the benefits of using a single-pixel camera for the acquisition. Indeed, a future improvement in this method would be to decrease the acquisition times by using compressive sampling [37]. By combining compressive sensing and constant improvements of the detection and computational resources, recovery of the 3D shape of hidden moving objects with high spatial resolution should be possible.

ACKNOWLEDGMENTS

We acknowledge support from the Royal Academy of Engineering under the Research Fellowship scheme Grant No. RF201617/16/31 and EPSRC, United Kingdom Grant No. EP/M01326X/1. This work has received funding from the European Union's Horizon 2020 research and innovation programme under Grant No. 801060.

[1] D. Faccio and A. Velten, A trillion frames per second: The techniques and applications of light-in-flight photography, Rep. Progr. Phys. **81**, 105901 (2018).

[2] A. Sume, M. Gustafsson, A. Jänis, S. Nilsson, J. Rahm, and A. Örbom, in *Radar Sensor Technology XIII* (International Society for Optics and Photonics, Orlando, Florida, USA, 2009), vol. 7308, p. 73080V.

[3] O. Katz, E. Small, and Y. Silberberg, Looking around corners and through thin turbid layers in real time with scattered incoherent light, Nat. Photonics **6**, 549 (2012).

[4] O. Katz, P. Heidmann, M. Fink, and S. Gigan, Non-invasive single-shot imaging through scattering layers and around corners via speckle correlations, Nat. Photonics **8**, 784 (2014).

[5] Y. Altmann, S. McLaughlin, M. J. Padgett, V. K. Goyal, A. Hero, and D. Faccio, Quantum-inspired computational imaging, Science **361**, eaat2298 (2018).

[6] C. Saunders, J. Murray-Bruce, and V. K. Goyal, Computational periscopy with an ordinary digital camera, Nature **565**, 472 (2019).

[7] U. Wandinger, *Lidar—Range-Resolved Optical Remote Sensing of the Atmosphere* (Springer, New York, 2005).

[8] B. Schwarz, Lidar: Mapping the world in 3D, Nat. Photonics **4**, 429 (2010).

[9] A. Kirmani, T. Hutchison, J. Davis, and R. Raskar, Looking around the corner using ultrafast transient imaging, Int. J. Comput. Vis. **95**, 13 (2011).

[10] M. Buttafava, J. Zeman, A. Tosi, K. Eliceiri, and A. Velten, Non-line-of-sight imaging using a time-gated single photon avalanche diode, Opt. Express **23**, 20997 (2015).

[11] A. K. Pediredla, M. Buttafava, A. Tosi, O Cossairt, and A. Veeraraghavan, in *2017 IEEE International Conference on Computational Photography (ICCP)* (IEEE, Stanford, California, USA, 2017).

[12] A. Velten, T. Willwacher, O. Gupta, A. Veeraraghavan, M. G. Bawendi, and R. Raskar, Recovering three-dimensional shape around a corner using ultrafast time-of-flight imaging, Nat. Commun. **3**, 745 (2012).

[13] G. Gariepy, F. Tonolini, R. Henderson, J. Leach, and D. Faccio, Detection and tracking of moving objects hidden from view, Nat. Photonics **10**, 23 (2016).

[14] S. Chan, R. E. Warburton, G. Gariepy, J. Leach, and D. Faccio, Non-line-of-sight tracking of people at long range, Opt. Express **25**, 10109 (2017).

[15] V. Arellano, D. Gutierrez, and A. Jarabo, Fast back-projection for non-line of sight reconstruction, Opt. Express **25**, 11574 (2017).

[16] C. Jin, J. Xie, S. Zhang, Z. Zhang, and Y. Zhao, Reconstruction of multiple non-line-of-sight objects using back projection based on ellipsoid mode decomposition, Opt. Express **26**, 20089 (2018).

[17] J. Klein, C. Peters, J. Martin, M. Laurenzis, and M. B. Hullin, Tracking objects outside the line of sight using 2D intensity images, Sci. Rep. **6**, 32491 (2016).

[18] P. Caramazza, A. Boccolini, D. Buschek, M. Hullin, C. F. Higham, R. Henderson, R. Murray-Smith, and D. Faccio, Neural network identification of people hidden from view with a single-pixel, single-photon detector, Sci. Rep. **8**, 11945 (2018).

[19] M. OToole, D. Lindell, and G. Wetzstein, Confocal non-line-of-sight imaging based on the light-cone transform, Nature **555**, 338 (2018).

[20] M. La Manna, F. Kine, E. Breitbach, J. Jackson, T. Sultan, and A. Velten, Error backprojection algorithms for non-line-of-sight imaging, IEEE Trans. Pattern Anal. Mach. Intell. **41**, 1615 (2018).

[21] A. C. Kak, Algorithms for reconstruction with nondiffracting sources, Principles Comput. Tomogr. Imaging, 49 (2001).

[22] M. P. Edgar, G. M. Gibson, and M. J. Padgett, Principles and prospects for single-pixel imaging, Nat. Photonics **13**, 13 (2019).

[23] N. Radwell, K. J. Mitchell, G. M. Gibson, M. P. Edgar, R. Bowman, and M. J. Padgett, Single-pixel infrared and visible microscope, Optica **1**, 285 (2014).

[24] E. Tajahuerce, V. Durán, P. Clemente, E. Irles, F. Soldevila, P. Andrés, and J. Lancis, Image transmission through dynamic scattering media by single-pixel photodetection, Opt. Express **22**, 16945 (2014).

[25] W. L. Chan, K. Charan, D. Takhar, K. F. Kelly, R. G. Baraniuk, and D. M. Mittleman, A single-pixel terahertz imaging system based on compressed sensing, Appl. Phys. Lett. **93**, 121105 (2008).

[26] G. M. Gibson, B. Sun, M. P. Edgar, D. B. Phillips, N. Hempler, G. T. Maker, G. P. Malcolm, and M. J. Padgett, Real-time imaging of methane gas leaks using a single-pixel camera, Opt. Express **25**, 2998 (2017).

[27] M. J. Sun, M. P. Edgar, G. M. Gibson, B. Sun, N. Radwell, R. Lamb, and M. J. Padgett, Single-pixel three-dimensional imaging with time-based depth resolution, Nat. Commun. **7**, 12010 (2016).

[28] M. P. Edgar, M. J. Sun, G. M. Gibson, G. C. Spalding, D. B. Phillips, and M. J. Padgett, in *Optical Trapping and Optical Micromanipulation XIII* (International Society for Optics and Photonics, San Diego, California, USA, 2016), vol. 9922, p. 99221B.

[29] M. F. Duarte, M. A. Davenport, D. Takhar, J. N. Laska, T. Sun, K. F. Kelly, and R. G. Baraniuk, Single-pixel imaging via compressive sampling, IEEE Signal Process. Mag. **25**, 83 (2008).

[30] M. Satat, G. Tancik, and R. Raskar, Lensless imaging with compressive ultrafast sensing, IEEE Trans. Comput. Imaging **3**, 398 (2017).

[31] R. A. Brooks, G. H. Weiss, and A. J. Talbert, A new approach to interpolation in computed tomography, J. Comput. Assist. Tomogr. **2**, 577 (1978).

[32] M. Sanzaro, P. Gattari, F. Villa, A. Tosi, G. Croce, and F. Zappa, Single-photon avalanche diodes in a 0.16 μm BCD technology with sharp timing response and red-enhanced sensitivity, IEEE J. Sel. Top. Quantum Electron. **24**, 1 (2018).

[33] P. Caramazza, K. Wilson, G. Gariepy, J. Leach, S. McLaughlin, D. Faccio, and Y. Altmann, Enhancing the recovery of a temporal sequence of images using joint deconvolution, Sci. Rep. **8**, 5257 (2018).

[34] M. A. T. Figueiredo and J. M. Bioucas-Dias, Restoration of Poissonian images using alternating direction optimization, IEEE Trans. Image Process. **19**, 3133 (2010).

[35] Y. Altmann, A. Maccarone, A. Halimi, A. McCarthy, G. Buller, and S. McLaughlin, in *2016 Sensor Signal Processing for Defence (SSPD)* (IEEE, Edinburgh, UK, 2016), p. 1.

[36] R. Tobin, Y. Altmann, X. Ren, A. McCarthy, R. Lamb, S. McLaughlin, and G. Buller, Comparative study of sampling strategies for sparse photon multispectral lidar imaging: Towards mosaic filter arrays, J. Opt. **19**, 094006 (2017).

[37] Q. Chen, S. K. Chamoli, P. Yin, X. Wang, and X. Xu, Imaging of hidden object using passive mode single pixel imaging with compressive sensing, Laser Phys. Lett. **15**, 126201 (2018).